Acta Crystallographica Section A
Foundations of Crystallography
ISSN 0108-7673

Received 9 July 2004
Accepted 24 January 2005

Solving non-centrosymmetric two-dimensional crystal structures by dynamic electron diffraction

Christoph T. Koch

Max Planck Institut für Metallforschung, Heisenbergstrasse 3, 70569 Stuttgart, Germany.
Correspondence e-mail: koch@mf.mpg.de

Despite the fast increase in expertise developed in the field of electron crystallography, dynamic scattering effects still remain a severe obstacle in this field, a hurdle that is being circumvented rather than fully tackled. In this paper, a new way of straightforward interpretation of conventional many-beam zone-axis dynamical electron diffraction patterns is presented that helps to solve the phase problem for non-centrosymmetric two-dimensional crystal structures, in particular if these contain only a few heavier atoms. While the implementation of this method is easiest for fairly weak multiple scattering, its extension to arbitrarily strong dynamical effects is mentioned. A method to obtain high-resolution diffraction data in the presence of specimen bending is proposed.

One of the properties of electron scattering is its approximately 10^3 times greater scattering cross section over X-rays. Together with the focusability of the electron beam by electromagnetic lenses, this means that much smaller objects (laterally and also in the beam direction) can be studied by electron beams than with X-rays or neutrons. However, multiple scattering, a 'side effect' of the large scattering cross section, is feared by many to distort the data, putting the use of conventional methods for structure determination in jeopardy, since, apart from recent developments, all of them are based on the single scattering approximation. For this reason, high electron beam energies, thin crystals and even precessing illumination (Marks & Sinkler, 2003) are used in order to avoid dynamic scattering effects, despite the fact that it is well known that 'high orders of interaction eliminate the ambiguities inherent in single scattering and enhance the sensitivity to structural detail' (Moodie & Fehlmann, 1993).

Attacks on the inversion problem in dynamic scattering theory have a long history (Allen *et al.*, 1998; Spence *et al.*, 1999; Rez, 1999). However, I will show that the complicated multiple scattering equations can be approximated by very simple ones for two-dimensional crystals, and that the presence of dynamic scattering can drastically simplify the structure-solving process in the presence of medium–heavy atoms in a 'sea' of lighter ones.

Prominent examples of such two-dimensional structures are proteins that crystallize in monolayers as well as the phospholipid bilayers they are embedded in when in their native state. Biological cell membranes defining the interfaces between cells, the building blocks of living organisms, and in eukaryotic cells also their subcompartments, are essential for making life, as we know it, possible. About 40% of the sequenced genes appear to code for membrane proteins, yet only 40 membrane protein structures are available at atomic resolution (Engel, 2003). Surface membranes found on all cells and the membranes that line eukaryotic organelles have the same basic architecture: a phospholipid bilayer. While atomic force microscopy (AFM) is being applied to the study of surfaces of such two-dimensional crystals, transmission electron microscopy is the only method capable of studying their inner structure in their functional state [see recent reviews by Glaeser & Downing (1993) and Engel (2003)] or when crystallized in two dimensions.

The 20 amino acids forming the basis for all proteins consist of H ($Z = 1$), C ($Z = 6$), N ($Z = 7$) and O ($Z = 8$) atoms. Only two of them (cysteine and methionine) contain an S ($Z = 16$) atom. Assuming the proteins encoded by the yeast genome to represent the 'typical' eukaryotic protein, the sulfur-containing amino acids are rather rare and together with tryptophan they make up less than 5% of the amino acids in a protein (Lodish *et al.*, 2000), *i.e.* there is about 1 S atom per every 30 amino acids or 3400 Da of protein molecular weight, which corresponds to 15 S atoms in a 51000 Da protein. Example calculations in this work will therefore focus on organic structures, demonstrating its potential usefulness in this field.

Recently, approaches that use the sensitivity of multiply scattered beams to structure-factor phases have proven useful in X-ray scattering near three-beam points (Chang, 1982; Juretschke, 1982; Shen, 1997). Apart from grazing-incidence geometry (Chang *et al.*, 1998), diffraction from two-dimensional crystals does not allow the selection of such three-beam conditions since the relrods in reciprocal space normal to the specimen surface are continuous and the crystal shape function in that direction is sharply peaked (zero excitation error) at the intersection of the Ewald sphere with the relrods (see Fig. 1). This means that every point in the two-dimensional crystal lattice will contribute to the multiple scattering process, independently of crystal tilt. Since their effective wavelength is proportional to $1/\cos(\theta)$ (θ = angle between the direction of

the incident electron beam and the surface normal), bulk-structure-probing electrons will be subject to very strong dynamic scattering and absorption for grazing incidence. In the remainder of this paper, it will be demonstrated that a large number of beams participating in the multiple scattering process is actually desirable, which is why the zone-axis case will be used for demonstration.

Defining modified three-dimensional structure factors

$$U'_{\mathbf{g}} = tU_{\mathbf{g}} = \frac{1}{|\mathbf{a}\times\mathbf{b}|}\sum_{j=1}^{N_{\rm atom}} f_j(|\mathbf{g}|/2)\exp(2\pi i\mathbf{r}_j\cdot\mathbf{g})$$

[**a** and **b** are unit-cell vectors in the plane of the crystal, $f_j(s=|\mathbf{g}|/2)$ are the electron scattering factors and r_j the positions of the atoms in a unit cell, and t is the specimen thickness], we may, using a recent expansion of the matrix exponential of the sum of two matrices (Koch & Spence, 2003), write down a 'scattering-path' expansion of the Bloch-wave multiple scattering formalism (Humphreys, 1979), which expands the dynamic electron wavefunction $\Psi_{\mathbf{g}}$ at the reciprocal-lattice point **g** in all contributing *Umweg* excitation paths. These paths may involve just the reciprocal-lattice point **g** (single scattering), the lattice points **h** and $\mathbf{g}-\mathbf{h}$ (double scattering), or **k**, $\mathbf{h}-\mathbf{k}$ and $\mathbf{g}-\mathbf{h}$ (triple scattering), or even longer paths. Since the crystal is non-periodic in the **z** direction and exactly one unit cell thick, we can define the unit-cell vector **c** to be normal to the plane defined by **a** and **b**. The unit-cell volume is then $\Omega = (\mathbf{a}\times\mathbf{b})\cdot\mathbf{c} = |\mathbf{a}\times\mathbf{b}|t$, even for triclinic unit cells.

Owing to the low density of most organic specimens, the scattering order needed to approximate the dynamic scattering sufficiently is rather low. The contribution of the single scattering path to the scattered electron wavefunction is (Koch & Spence, 2003)

$$\Psi^{(1)}_{\mathbf{g}} = \begin{cases} \dfrac{U'_{\mathbf{g}}}{t}\dfrac{\exp(i\pi t\zeta_{\mathbf{g}}/k_n)-1}{\zeta_{\mathbf{g}}}, & \zeta_{\mathbf{g}}\neq 0 \\ \dfrac{U'_{\mathbf{g}}}{t}\dfrac{i\pi t}{k_n} = U'_{\mathbf{g}}\dfrac{i\pi}{k_n}, & \zeta_{\mathbf{g}} = 0. \end{cases} \qquad (1)$$

$\zeta_{\mathbf{g}} = k^2 - (\mathbf{k}+\mathbf{g})^2 \approx 2k_n s_{\mathbf{g}}$, where $s_{\mathbf{g}}$ is the excitation error, *i.e.* the distance along the relrod between the Ewald sphere and the reciprocal-lattice point **g**. **k** is the incident wavevector ($|\mathbf{k}| = k = 1/\lambda$) and k_n is the component of the incident electron wavevector normal to the crystal surface, *i.e.* anti-parallel to **c**.

In order to properly account for the presence of the two surfaces of a two-dimensional crystal, we must add two semi-infinite slabs of vacuum to both top and bottom of the structure, thus taking the limit $t\to\infty$. It then becomes very clear from (1) that, if $U'_{\mathbf{g}}$ varies smoothly with g_z, all terms with $\zeta_{\mathbf{g}}\neq 0$ have negligible contributions because of their inverse proportionality to the thickness t. This is equivalent to the fact that the scattering potential of two-dimensional crystals is continuous in the z direction, and can therefore be intersected by the Ewald sphere, as has already been mentioned.

Using the general expression from Koch & Spence (2003), we see that the same is true for all the higher-order scattering contributions as well. We may thus write the multiple scattering expansion as

$$\begin{aligned}\Psi_{\mathbf{g}} &= \sum_{j=0}^{\infty}\Psi^{(j)}_{\mathbf{g}} \\ &= \delta_{\mathbf{g}} + \sum_{j=1}^{\infty}\frac{1}{j!}\left(\frac{i\pi}{k_n}\right)^j \\ &\quad\times\sum_{g_1}\sum_{g_2}\cdots\sum_{g_{j-2}}\sum_{g_{j-1}} U'_{\mathbf{g}-\mathbf{g}_1}U'_{\mathbf{g}_1-\mathbf{g}_2}\cdots U'_{\mathbf{g}_{j-2}-\mathbf{g}_{j-1}}U'_{\mathbf{g}_{j-1}}, \qquad (2)\end{aligned}$$

where each of the sums is over all reciprocal-lattice points on the Ewald sphere. Although slightly different for finite crystals, the multiple scattering expansions derived by Fujiwara (1959) and earlier by Cowley & Moodie (1957) converge exactly to this result for the special case treated here.

Since all the relrods intersect the Ewald sphere, each of the sums is equivalent to a convolution of the array of $U'_{\mathbf{g}}$ with another copy of itself. The two-dimensional scattered electron wavefunction can therefore be written in real space as

$$\tilde{\Psi}(\mathbf{r}) = {\rm FT}(\Psi_{\mathbf{g}}) \approx \sum_{j=0}^{\infty}\frac{1}{j!}\left(\frac{i\pi}{k_n}\right)^j\Phi(\mathbf{r})^j = \exp\left(\frac{i\pi}{k_n}\Phi(\mathbf{r})\right), \qquad (3)$$

where $\Phi(r) = {\rm FT}(U'_{\mathbf{g}})$, *i.e.* the two-dimensional Fourier transform of the array of reciprocal-lattice points on the Ewald sphere. In the limit of zero wavelength ($|\mathbf{k}|\to\infty$, perfectly flat Ewald sphere), $\Phi(\mathbf{r})$ is proportional to the potential of the unit cell projected along the direction of the incident electron beam. The only difference in this expression from the classical phase-object approximation is that it includes the curvature of the Ewald sphere. The '$\approx$' relation has been used because, strictly speaking, the convolution theorem is only exact for periodic objects. Although the surface of the Ewald sphere may be looked at as being periodic, it is not periodic in the Cartesian coordinate system, nor does the high-energy approximation in the Bloch-wave formalism used here include any back scattering of electrons.

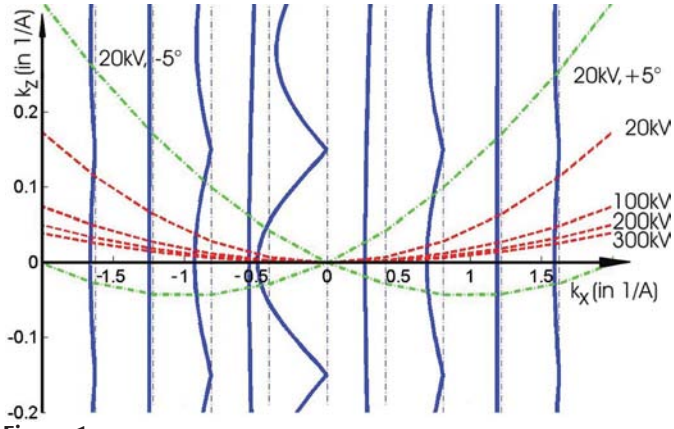

Figure 1
Modulus of the scattering potential $U_{\mathbf{g}}$ for a two-dimensional graphite crystal (a = 2.46, c = 6.7 Å), which has a thickness of one unit cell, *i.e.* two graphene sheets. The reciprocal-space lattice is continuous normal to the crystal surface. Zone-axis Ewald-sphere sections for 20, 100, 200, 300 kV, as well as for 20 kV with beam tilts of ±5° are shown.

The inverse Fourier transform of the diffraction pattern is then

$$\begin{aligned}\mathrm{FT}^{-1}(I_{\mathbf{g}}) &= \mathrm{FT}^{-1}(\Psi_{\mathbf{g}}\Psi_{\mathbf{g}}^{*}) \\ &\approx \tilde{\Psi}(\mathbf{r}) \otimes \tilde{\Psi}(-\mathbf{r}) \\ &= 1 + i\left(\frac{\pi}{k_n}\right)[\Phi(\mathbf{r}) \otimes 1 - 1 \otimes \Phi(-\mathbf{r})^{*}] + \left(\frac{\pi}{k_n}\right)^{2} \\ &\quad \times [-\Phi^{2}(\mathbf{r}) \otimes 1 - 1 \otimes \Phi^{2}(-\mathbf{r})^{*} + \Phi(\mathbf{r}) \otimes \Phi(-\mathbf{r})^{*}] \\ &\quad + \frac{i}{2}\left(\frac{\pi}{k_n}\right)^{3}[-\Phi^{3}(\mathbf{r}) \otimes 1 + 1 \otimes \Phi^{3}(-\mathbf{r})^{*} \\ &\quad + \Phi^{2}(\mathbf{r}) \otimes \Phi(-\mathbf{r})^{*} - \Phi^{2}(-\mathbf{r})^{*} \otimes \Phi(\mathbf{r})] + O\left(\frac{\pi}{k_n}\right)^{4} \\ &= P^{(\mathrm{re})}(\mathbf{r}) + iP^{(\mathrm{im})}(\mathbf{r}). \end{aligned} \tag{4}$$

All the terms involving the correlation with the constant array 1 are constants and do not produce any spatially varying contribution in the real or imaginary part of $\mathrm{FT}^{-1}(I_{\mathbf{g}})$. The auto-correlation function

$$\Phi(\mathbf{r}) \otimes \Phi(-\mathbf{r})^{*} = \int_{\text{unit cell area}} \Phi(\mathbf{r}')\Phi(\mathbf{r}-\mathbf{r}')^{*}\,\mathrm{d}^{2}r'$$

is real for any general real $\Phi(\mathbf{r})$. The first non-zero contribution to the imaginary part of $\mathrm{FT}^{-1}(I_{\mathbf{g}})$ stems from the 1.5-fold scattering defined by the terms in the last line of the expression above, which is the product of the first- order ($\Psi_{\mathbf{g}}^{(1)}$) and second-order Born approximation terms ($\Psi_{\mathbf{g}}^{(2)}$) in expressions (2) and (3).

Once the only means for structure determination, the Patterson function has lost its importance in solving large protein structures (Dorset, 1995). This is due to two reasons: (i) N atoms per unit cell produce $N^2 - N$ peaks in the Patterson function and (ii) the advantage of electron radiation over X-rays in its sensitivity to light atoms reduces the 'scattering power' of heavy atoms so that peaks due to heavy–light-atom distances are not as clearly identifiable as in X-ray diffraction.

Another reason why Patterson maps are difficult to use for larger molecules is their poor resolution. It is limited to the largest scattering vector present in the as-measured diffraction pattern. Since only the scattering intensity can be measured, the noise level increases linearly with the magnitude of the structure factor, making it difficult to obtain diffraction data at high resolution. Since already the first term of $P^{(\mathrm{im})}$ consists of scattering paths of length 2, it includes linear contributions from structure factors that lie outside the range of measured spots. As already mentioned, even the first term of $P^{(\mathrm{im})}$ is scaled with an additional π/k_n factor. Any structure factor whose magnitude is larger than π/k_n ($= \pi * \lambda$ for normal incidence) will contribute with a better signal/noise ratio to $P^{(\mathrm{im})}$ than to $P^{(\mathrm{re})}$, if only first- and 1.5-order scattering events are considered. Structure factors at very large reciprocal-lattice vectors may have their strongest contribution at even higher scattering orders if the product of wavelength and specimen thickness is large enough. This means that, in principle, using higher scattering orders gives us access to higher spatial resolution, even beyond the range of measured diffraction spots.

Furthermore, the asymmetry of $P^{(\mathrm{im})}$ removes the strong central peak due to the sum of isolated atom scattering potentials [first- and second-order terms in expression (4)], which often drowns peaks in the Patterson function corresponding to short interatomic vectors.

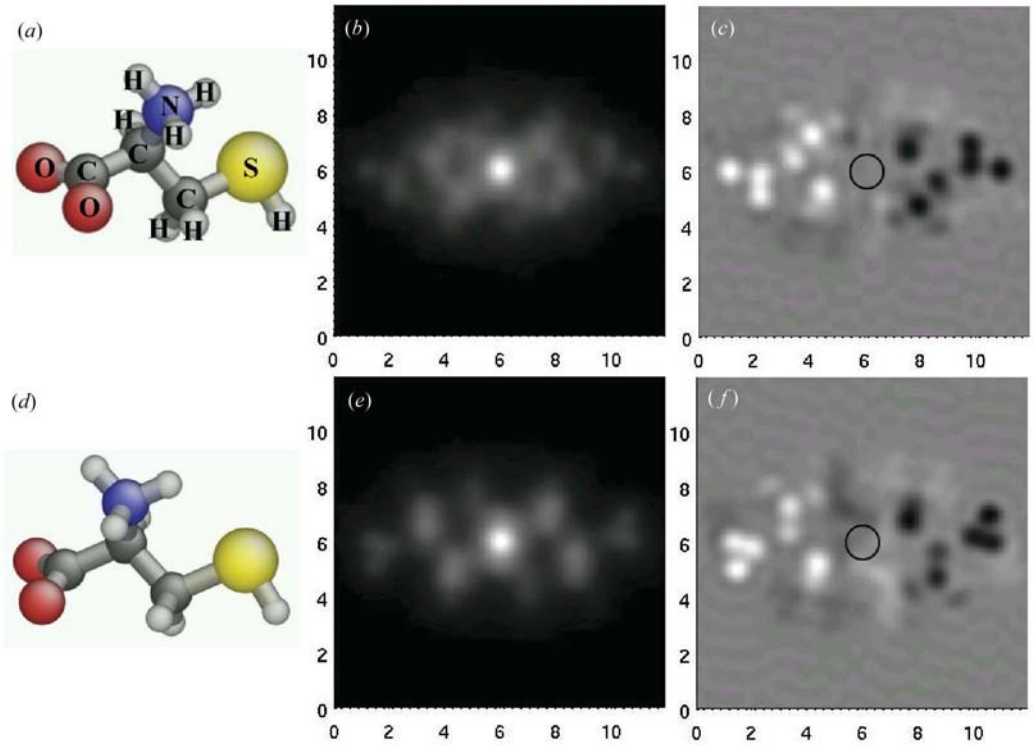

Figure 2
(*a*) Model of L-cysteine. (*b*) $P^{(\mathrm{re})}$ real part of Fourier transform of diffraction pattern (Patterson function). (*c*) $P^{(\mathrm{im})} = -P^{(\mathrm{im})}(-\mathbf{r})$. The black circle in the center indicates the position of the S atom, which is not visible because it sits at the center and is itself symmetric. (*d*)–(*f*) same as (*a*)–(*c*), but with rotation of the molecule by 30° about the *y* axis. The model has been placed in an artificial 12 × 12 Å unit cell for simulating the diffraction patterns. The simulation includes first-, second- and third-order scattering. Diffraction data up to a real-space resolution of 1.15 Å are included. The parameterized scattering factors by Doyle & Turner (1968) have been used, also for Figs. 1, 3 and 5.

Fig. 2 demonstrates the increased sharpness of features in $P^{(\mathrm{im})}$ *versus* $P^{(\mathrm{re})}$. $P^{(\mathrm{im})}$ is also very easy to interpret without using any of the standard Patterson deconvolution techniques. It allows a direct interpretation of the asymmetric part of the structure. Although some contrast produced by vectors between lighter atoms, such as O, N or C, is discernible, the contrast due to the S atom and its lighter neighbors dominates, *i.e.* one may speak of $P^{(\mathrm{im})}$ as being produced by the S atom. Even the peaks corresponding to S–H vectors dominate over those produced by atom pairs that do not involve sulfur. If single atomic positions can be resolved, only a few tilt angles are necessary to reconstruct the three-dimensional structure, otherwise standard tomographic methods must be used. However, one should take care to correct for Ewald-sphere curvature effects, as will be discussed below. Once the asymmetric part of the structure has been determined, it can be used to deconvolve $P^{(\mathrm{re})}$ to obtain the symmetric part. The presence of several heavier atoms in the structure will lead to a superposition of $P^{(\mathrm{im})}$ 'seen' from the point of view of each one of them. Disulfide bonds, for example, may therefore produce very distinct double peaks if their projected distance can be resolved.

In order to show the enhancement in resolution more clearly, a one-dimensional test structure with different atomic spacings has been used in simulations. The structure consists of one S and three C atoms (see Fig. 3*a*), where $\phi(\mathbf{r})$ is scaled to volts (m = mass of electron, e = charge of electron, h = Planck's constant). The distance between the two rightmost C atoms is 1.5 Å. The diffraction has been simulated using the simple phase-object approximation for an electron-beam accelerating voltage of 10 kV, neglecting Ewald-sphere curvature effects.

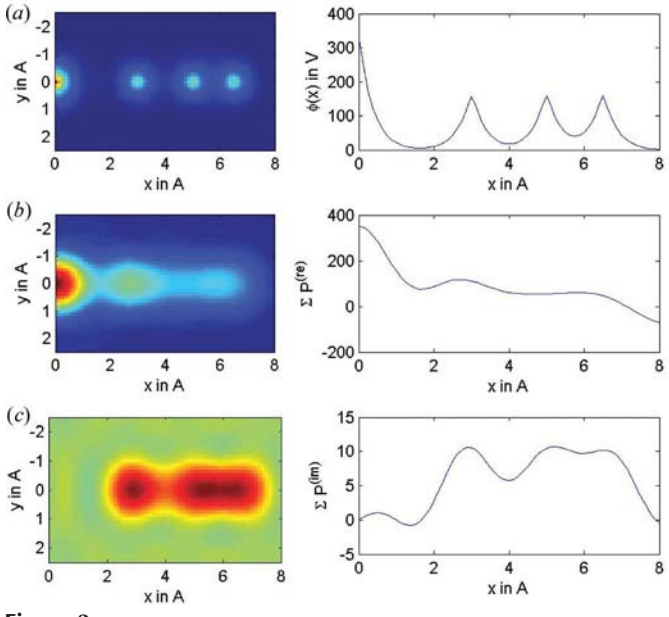

Figure 3
(*a*) Potential $[h^2/r2\pi m|e|\phi(\mathbf{r})]$ of a one-dimensional test structure consisting of one S and three C atoms at positions $x = 0$, 3, 5 and 6.5 Å, respectively. Both the two-dimensional potential map as well as a line scan along its axis of symmetry are shown. (*b*) The Patterson map $P^{(\mathrm{re})}$ and its sum perpendicular to its axis of symmetry. (*c*) $P^{(\mathrm{im})}$ and its sum perpendicular to its axis of symmetry. The last two C atoms with a spacing of 1.5 Å between them are clearly resolved. The diffraction data giving rise to both $P^{(\mathrm{re})}$ and $P^{(\mathrm{im})}$ have been limited to a real-space resolution of 1.78 Å using a top hat aperture function.

Since $P^{(\mathrm{re})}(\mathbf{r})$ (Fig. 3*b*) is primarily a function of structure factors $U_{\mathbf{g}}$ for $|\mathbf{g}| < (1.78\ \text{Å})^{-1}$, the 1.5 Å spacing between the rightmost two C atoms cannot be resolved, and only a maximum at a position between $x = 5$ and $x = 6.5$ Å is visible. The higher scattering order and thus higher-resolution contributions to $P^{(\mathrm{im})}(\mathbf{r})$ (Fig. 3*c*), however, allow a clear distinction between the two atomic positions.

Besides dynamic scattering effects, the curvature of the Ewald sphere and, especially for two-dimensional organic crystals, film bending are major issues in the interpretation of high-resolution electron scattering data. Aside from the insensitivity of diffraction data to lens aberrations, one of the major advantages of using reciprocal-space information over images is the constructive interference in the diffraction spots produced by a crystalline specimen. By using highly coherent field-emitting electron sources, even weak high-order reflections may be recorded with good signal-to-noise ratio. However, this can only be done if the specimen is flat over the area illuminated by the electron beam. If the convergence angle of the incident electron beam, the vertical position of the specimen with respect to that of the focused electron probe, and the camera length are controlled, the area of the specimen scattering into a single pixel of the recording medium should be small enough to be considered flat. The definition of 'flat' depends on the desired resolution, however, more stringent requirements may apply for interpreting the asymmetries in the diffraction pattern than for the application of kinetic scattering theory. Under carefully designed experimental conditions, it has recently been possible to record convergent-beam electron diffraction (CBED) patterns of beam-sensitive organic material (Wu & Spence, 2002). In addition to spot fading of radiation-sensitive material, the obtainable resolution of the diffraction data is also limited by the amount of film bending and the combination of the above-mentioned parameters.

Fig. 4 illustrates the experimental set-up for CBED from a bent specimen. Different regions on the specimen are illuminated with different illumination angles and recorded inde-

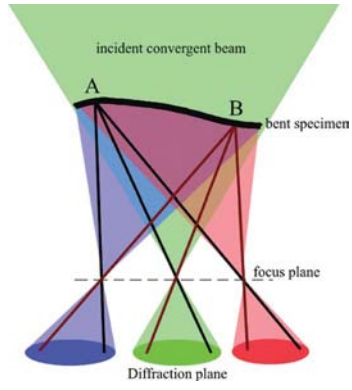

Figure 4
Diagram of convergent illumination of a bent specimen.

pendently using charge-coupled detectors (CCD), image plates or film. The size of the illuminating spot may be larger than the specimen, in which case the outline of the specimen will be superimposed on each diffraction disc, making it possible to map exactly the direction of the incident electron beam to the specimen position. In the presence of film bending, classical bent contours will appear across these shadow images within each disc. By moving the convergent probe and recording a second pattern, one can determine the local orientation by comparing the set of diffraction intensities across the specimen.

Example: the electron beam is normal to the specimen surface at points A and B in Fig. 4, but not at all the points between A and B. The diffraction patterns of the areas around points A and B are recorded in a single detector pixel per diffraction spot and are, apart from noise, equivalent. They may thus be added together to increase the signal/noise ratio by a factor of $2^{1/2}$. Parallel illumination of the whole specimen would produce coherent interference of diffraction patterns corresponding to different film orientations and would therefore not be a truly representative diffraction pattern. Moving the electron beam will change the local illumination angle at points A and B, causing their diffraction patterns to differ in a very well defined way, because the change in local illumination angle depends on the probe position and is thus known. However, they will now agree with the diffraction patterns from different areas of the specimen. The local film orientation can now be mapped everywhere using these two data sets.

The method of using higher-order scattering described in this paper is, strictly speaking, only correct for electrons that are incident normal to the specimen surface because even kinematic theory predicts asymmetries of diffraction patterns if a curved Ewald sphere intersects crystal truncation rods in non-normal incidence geometries. These kinematic asymmetries will bring additional terms to contribute to $P^{(\mathrm{im})}(\mathbf{r})$. However, Fig. 5 demonstrates that, if we use the difference of two diffraction patterns $I_{\mathrm{diff}}(\mathbf{g})$ of opposite tilt angle

$$I_{\mathrm{diff}}(\mathbf{g}) = I(+\theta, \mathbf{g}) - I(-\theta, -\mathbf{g}), \qquad (5)$$

these kinematic asymmetries are removed but the dynamic terms enhanced in $P^{(\mathrm{im})}(\mathbf{r})$.

Fig. 5 shows the reconstruction of the cysteine structure from Fig. 2 for a deviation from surface normal incidence of $\theta = -20^\circ$ (*a*), 0° (*c*) and $+20^\circ$ (*b*). Reconstructing each of the tilted diffraction patterns will introduce artefacts due to kinematical asymmetries (*e.g.* see arrow in Fig. 5*b*), but reconstructing the difference [see expression (5)] of these two diffraction patterns removes these artefacts, showing good agreement with the reconstruction of the $\theta = 0^\circ$ data (Fig. 5*c*). The origin of kinematical asymmetries can easily be seen from the tilted Ewald sphere sections in Fig. 1. The structure-factor moduli $|U_{\mathbf{g}}(+\theta)|$ and $|U_{\mathbf{g}}(-\theta)|$ differ: the curved Ewald sphere causes $|\mathbf{g}| \neq |-\mathbf{g}|$, while $|U_{\mathbf{g}}(+\theta)| = U_{-\mathbf{g}}(-\theta)|$, θ being the angle between the specimen surface normal of the electron-beam direction. The restored asymmetric potential map is now the sum of two potential maps obtained by projecting the cysteine structure with $\theta = \pm 20^\circ$, as can be seen by the double appearance of the O atom indicated by the two arrows in Fig. 5*d*). Although the area of the specimen coherently scattering into a single diffraction pattern has been reduced in order to circumvent film bending, diffraction patterns from a much larger area can be recorded simultaneously. These patterns can then be added up incoherently while correcting for their tilt angle, thus providing a maximum of information and signal/noise from a single diffraction pattern, since the coherence conditions can be adjusted with several parameters (specimen height, convergence angle and camera length/pixel size of recording medium) to match the experimental conditions (desired resolution, radiation sensitivity and amount of film bending).

If a tomographic series of diffraction patterns is to be reconstructed, the fact that projections of two oppositely tilted structures are always obtained should be taken into account, requiring a modification of the standard tomographic reconstruction algorithms.

The fact that the application of kinematic scattering theory for electron diffraction of the type of structures discussed in this work has proven very successful poses the question about the strength and thus the detectability of the multiple scattering needed for this analysis. Some preliminary tests including random noise have shown that the signal-to-noise ratio must be better than that needed for the conventional

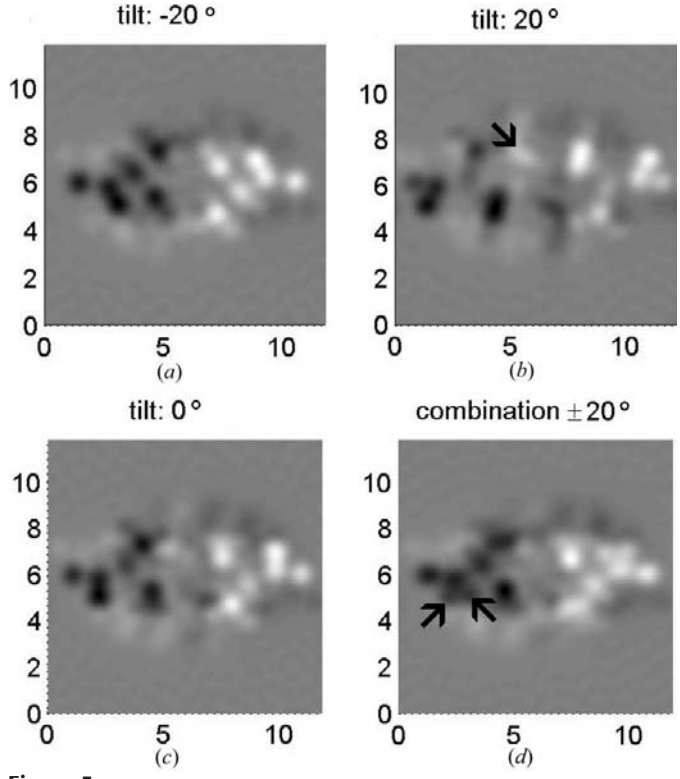

Figure 5
(*a*) $P^{(\mathrm{im})}(\mathbf{r})$ of the cysteine structure shown in Fig. 2 for an accelerating voltage of 5 kV and a beam tilt of $\theta = -20^\circ$. (*b*), (*c*) $P^{(\mathrm{im})}(\mathbf{r})$ for a beam tilt of $\theta = +20^\circ$ and $\theta = 0^\circ$, respectively. (*d*) $P^{(\mathrm{im})}(\mathbf{r})$ obtained from $I_{\mathrm{diff}}(\mathbf{g}) = I(+\theta, \mathbf{g}) - I(-\theta, -\mathbf{g})$; the signal is also almost twice as strong as in (*a*)–(*c*).

analysis of diffraction patterns as one would expect. Since $P^{(\mathrm{im})}$ is composed entirely of the asymmetric part of the diffraction pattern, the noise must be considerably less than the differences in intensities between Friedel mates. Systematic Friedel differences as large as 40% have been observed experimentally in diffraction patterns of bacteriorhodopsin at 20 kV, reducing to 10% at 120 kV (Glaeser & Ceska, 1989), a fact that is very obvious from equation (4). The amount of dynamic scattering is thus very sensitive to the kinetic energy of the incident electrons. One might even consider fitting diffraction data recorded at different accelerating voltages with a polynomial in wavelength ($1/k_n \propto \lambda$). Using only the cubic portion would filter out the 1.5-fold scattering part in the presence of higher-order scattering. It may then even be advantageous to use the 2.5 or higher (non-integer-order) scattering since the peaks in $P^{(\mathrm{im})}$ become sharper with increasing scattering order. For thicker specimen and low enough voltage, such higher-order scattering will dominate the single scattering part. Since a quantitative analysis of the signal-to-noise ratio required for successful structure solving depends on the kinetic energy of the electrons, the size of the structure (in particular the portion of it that is asymmetric) and the required resolution, it is beyond the scope of this paper.

In summary, it has been shown that a multiple (dynamic) scattering interpretation of electron diffraction patterns of two-dimensional crystal structures may greatly assist in solving the phase problem, especially for the case of non-centrosymmetric structures containing only a few heavy atoms. The role of such 'heavy' atoms may even be played by sulfur or phosphorus already present in many organic structures such as proteins or phospholipid bilayers. However, for exploring the experimental merits of using the higher-order scattering terms, it may be best to start with heavy-atom-stained specimens whose phases can be solved for by conventional methods. These would allow higher accelerating voltages to be used and the effect of heavy-atom scattering power for phase determination in $P^{(\mathrm{im})}$ could directly be compared to that in $P^{(\mathrm{re})}$. In addition to a mathematical description of the method, ideas for obtaining diffraction data from a bent specimen and correcting for Ewald-sphere curvature artefacts have been presented.

The author would like to thank Professor J. C. H. Spence for the many very fruitful discussions that led to this work and also Professor M. Rühle for his very generous support.

References

Allen, L. J., Josefsson, T. W. & Leeb, H. (1998). *Acta Cryst.* A**54**, 388–398.
Chang, S. L. (1982). *Phys. Rev. Lett.* **48**, 163–166.
Chang, S. L., Huang, Y. S., Chao, C. H., Tang, M. T. & Stetsko, Y. P. (1998). *Phys. Rev. Lett.* **80**, 301–304.
Cowley, J. M. & Moodie, A. F. (1957). *Acta Cryst.* **10**, 609–619.
Dorset, D. L. (1995). *Structural Electron Crystallography*. New York: Plenum Press.
Doyle, P. A. & Turner, P. S. (1968). *Acta Cryst.* A**24**, 390–397.
Engel, A. (2003). *Histochem. Cell Biol.* **120**, 93–102.
Fujiwara, K. (1959). *J. Phys. Soc. Jpn*, **14**, 1513–1524.
Glaeser, R. M. & Ceska, T. A. (1989). *Acta Cryst.* A**45**, 620–628.
Glaeser, R. M. & Downing, K. H. (1993). *Ultramicroscopy*, **52**, 478–486.
Humphreys, C. J. (1979). *Rep. Prog. Phys.* **42**, 1825–1885.
Juretschke, H. (1982). *Phys. Rev. Lett.* **48**, 1487–1489.
Koch, C. T. & Spence, J. C. H. (2003). *J. Phys A: Math. Gen.* **36**, 803–816.
Lodish, H., Berk, A., Zirpursky, S. L., Matsudaira, P., Baltimore, D. & Darnell, J. E. (2000). *Molecular Cell Biology.* New York: W. H. Freeman and Co.
Marks, L. D. & Sinkler, W. (2003). *Microsc. Microanal.* **9**, 399–410.
Moodie, A. & Fehlmann, M. (1993). *Acta Cryst.* A**49**, 376–378.
Rez, P. (1999). *Acta Cryst.* A**55**, 160–167.
Shen, Q. (1997). *Phys. Rev. Lett.* **80**, 3268–3271.
Spence, J. C. H., Calef, B. & Zuo, J. M. (1999). *Acta Cryst.* A**55**, 112–118.
Wu, J. S. & Spence, J. C. H. (2002). *Acta Cryst.* A**58**, 580–589.